The Astrophysical Journal, 652:1059–1067, 2006 December 1
© 2006. The American Astronomical Society. All rights reserved. Printed in U.S.A.

STRUCTURE OF MAGNETIC TOWER JETS IN STRATIFIED ATMOSPHERES

Masanori Nakamura,[1] Hui Li,[1] and Shengtai Li[2]
Received 2006 June 7; accepted 2006 August 9

ABSTRACT

Using a new approach to modeling the magnetically dominated outflows from active galactic nuclei, we study the propagation of magnetic tower jets in gravitationally stratified atmospheres (such as a galaxy cluster environment) at large scales (more than tens of kiloparsecs) by performing three-dimensional MHD simulations. We present the detailed analysis of the MHD waves, the cylindrical radial force balance, and the collimation of magnetic tower jets. As magnetic energy is injected into a small central volume over a finite amount of time, the magnetic fields expand down the background density gradient, forming a collimated jet and an expanded "lobe" due to the gradually decreasing background density and pressure. Both the jet and lobes are magnetically dominated. In addition, the injection and expansion produce a hydrodynamic shock wave that moves ahead of and encloses the magnetic tower jet. This shock can eventually break the hydrostatic equilibrium in the ambient medium and cause a global gravitational contraction. This contraction produces a strong compression at the head of the magnetic tower front and helps to collimate the jet radially to produce a slender body. At the outer edge of the jet, the magnetic pressure is balanced by the background (modified) gas pressure, without any significant contribution from the hoop stress. On the other hand, along the central axis of the jet, hoop stress is the dominant force in shaping the central collimation of the poloidal current. The system, which possesses a highly wound helical magnetic configuration, never quite reaches a force-free equilibrium state, although the evolution becomes much slower at late stages. The simulations were performed without any initial perturbations, so the overall structures of the jet remain mostly axisymmetric.

Subject headings: galaxies: active — galaxies: jets — magnetic fields — methods: numerical — MHD

1. INTRODUCTION

A number of astronomical systems have been discovered to eject tightly collimated and hypersonic plasma beams and large magnetic fields into the interstellar, intergalactic, and intracluster medium from the central objects during their initial and/or final (often violent) stages. Magnetohydrodynamic (MHD) mechanisms are frequently invoked to model the launching, acceleration, and collimation of jets from young stellar objects, X-ray binaries, active galactic nuclei (AGNs), microquasars, and quasars (see, e.g., Meier et al. 2001 and references therein).

A theory of magnetically driven outflows in the electromagnetic regime has been proposed by Blandford (1976) and Lovelace (1976) and subsequently applied to rotating black holes (Blandford & Znajek 1977) and to magnetized accretion disks (Blandford & Payne 1982). By definition, these outflows initially are dominated by electromagnetic forces close to the central engine. In these and subsequent models of magnetically driven outflows (jets/winds), the plasma velocity passes successively through the sonic, slow-magnetosonic, Alfvénic, and fast-magnetosonic critical surfaces.

The first attempt to investigate the nonlinear (time dependent) behavior of magnetically driven outflows from accretion disks was performed by Uchida & Shibata (1985). The differential rotation in the system (central star/black hole and the accretion disk) creates a magnetic coil that simultaneously expels and pinches some of the infalling material. The buildup of the azimuthal (toroidal) field component in the accretion disk is released along the poloidal field lines as large-amplitude torsional Alfvén waves ("sweeping magnetic twist"). After this pioneering work, a number of numerical simulations to study the MHD jets were performed (see, e.g., Ferrari 1998 and references therein). An underlying large-scale poloidal field for producing the magnetically driven jets is almost universally assumed in many theoretical and numerical models. However, the origin and existence of such a galactic magnetic field are still poorly understood.

In contrast with the large-scale field models, Lynden-Bell (Lynden-Bell & Boily 1994; Lynden-Bell 1996, 2003, 2006) examined the expansion of the local force-free magnetic loops anchored to the star and the accretion disk by using the semianalytic approach. Twisted magnetic fluxes caused by the disk rotation make the magnetic loops unstable and splay out at a semiangle of 60° from the rotational axis of the disk. Global magnetostatic solutions of magnetic towers with external thermal pressure were also computed by Li et al. (2001) using the Grad-Shafranov equation in axisymmetry (see also Lovelace et al. 2002; Lovelace & Romanova 2003; Uzdensky & MacFadyen 2006). Full MHD numerical simulations of magnetic towers have been performed in two dimensions (axisymmetric; Romanova et al. 1998; Turner et al. 1999; Ustyugova et al. 2000; Kudoh et al. 2002; Kato et al. 2004) and three dimensions (Kato et al. 2004). Magnetic towers are also observed in laboratory experiments (Hsu & Bellan 2002; Lebedev et al. 2005).

This paper describes the nonlinear dynamics of propagating magnetic tower jets in large scales (more than tens of kiloparsecs) based on three-dimensional (3D) MHD simulations. We follow closely the approach described in Li et al. (2006, hereafter Paper I). Our approach in this paper is different from that in Paper I, in which we studied the dynamics of magnetic field evolution in a uniform background medium. In this paper we present results on the injection and the subsequent expansion of magnetic fields in a stably stratified background medium that is described by an isothermal King model (King 1962). Since the simulated magnetic structures traverse several scale heights of

[1] Theoretical Astrophysics, Los Alamos National Laboratory, MS B227, Los Alamos, NM 87545; nakamura@lanl.gov, hli@lanl.gov.
[2] Mathematical Modeling and Analysis, Los Alamos National Laboratory, MS B284, Los Alamos, NM 87545; sli@lanl.gov.

TABLE 1
Units of Physical Quantities for Normalization

Physical Quantities	Description	Normalization Units	Typical Values
R [$=(x^2+y^2+z^2)^{1/2}$]	Length	R_0	5 kpc
$\boldsymbol{V}$	Velocity field	C_{s0}	4.6×10^7 cm s^{-1}
t	Time	R_0/C_{s0}	1.0×10^7 yr
ρ	Density	ρ_0	5.0×10^{-27} g cm^{-3}
p	Pressure	$\rho_0 C_{s0}^2$	1.4×10^{-11} dyn cm^{-2}
$\boldsymbol{B}$	Magnetic field	$(4\pi\rho_0 C_{s0}^2)^{1/2}$	17.1 μG

Notes.—The initial values of the density ρ_0 and sound speed C_{s0} at the origin $(x, y, z) = (0, 0, 0)$ are chosen to be the typical density and velocity in the system. The initial dimensionless density ρ' and pressure p' at the origin are set to unity. We therefore have the initial dimensionless sound speed $C_s' = \gamma^{1/2} \approx 1.29$. A characteristic timescale, the initial sound crossing time $\tau_{s0} = R_0/C_{s0} = 10.0$ Myr, which corresponds to the dimensionless timescale $\tau \approx 0.78$.

the background medium, we believe that our simulations can be compared with the radio sources inside the galaxy cluster core regions. Due to limited numerical dynamic range, however, the injection region (see Paper I) assumed in this paper is large (a few kiloparsecs). Our goal here is to provide a detailed analysis of the magnetic tower jets, in terms of their MHD wave structures, their cylindrical radial force balance, and their collimation. The paper is organized as follows: In § 2, we outline the model and numerical methods. In § 3, we describe the simulation results. Discussions and conclusions are given in §§ 4 and 5, respectively.

2. MODEL ASSUMPTIONS AND NUMERICAL METHODS

The basic model assumptions and numerical treatments we adopt here are essentially the same as those in Paper I. Magnetic fluxes and energy are injected into a characteristic central volume over a finite duration. The injected fluxes are not force-free so that Lorentz forces cause them to expand, interacting with the background medium. For the sake of completeness, we show the basic equations and other essential numerical setup here again and refer readers to Paper I for more details.

2.1. *Basic Equations*

We solve the nonlinear system of time-dependent ideal MHD equations numerically in a 3D Cartesian coordinate system (x, y, z):

$$\frac{\partial \rho}{\partial t} + \nabla\cdot(\rho \boldsymbol{V}) = \dot{\rho}_{\rm inj}, \tag{1}$$

$$\frac{\partial(\rho \boldsymbol{V})}{\partial t} + \nabla\cdot\left(\rho \boldsymbol{V}\boldsymbol{V} + p + \frac{B^2}{2} - \boldsymbol{B}\boldsymbol{B}\right) = -\rho\nabla\psi, \tag{2}$$

$$\frac{\partial E}{\partial t} + \nabla\cdot\left[\left(E + p + \frac{B^2}{2}\right)\boldsymbol{V} - \boldsymbol{B}(\boldsymbol{V}\cdot\boldsymbol{B})\right] = -\rho\boldsymbol{V}\cdot\nabla\psi + \dot{E}_{\rm inj}, \tag{3}$$

$$\frac{\partial \boldsymbol{B}}{\partial t} - \nabla\times(\boldsymbol{V}\times\boldsymbol{B}) = \dot{\boldsymbol{B}}_{\rm inj}. \tag{4}$$

Here ρ, p, $\boldsymbol{V}$, $\boldsymbol{B}$, and E denote the mass density, hydrodynamic (gas) pressure, fluid velocity, magnetic field, and total energy, respectively. The total energy E is defined as $E = p/(\gamma - 1) + \rho V^2/2 + B^2/2$, where γ is the ratio of the specific heats (a value of 5/3 is used). The Newtonian gravity is $-\nabla\psi$. Quantities $\dot{\rho}_{\rm inj}$, $\dot{\boldsymbol{B}}_{\rm inj}$, and $\dot{E}_{\rm inj}$ represent the time-dependent injections of mass, magnetic flux, and energy, respectively, whose expressions are given in Paper I.

We normalize physical quantities with the unit length scale R_0, density ρ_0, and velocity V_0 in the system; other quantities are normalized as derived from their combinations, e.g., time as R_0/V_0. These normalizing factors are summarized in Table 1. Hereafter, we use the normalized variables throughout the paper. Note that a factor of 4π has been absorbed into the scaling for both the magnetic field $\boldsymbol{B}$ and the corresponding current density $\boldsymbol{J}$. To put our normalized physical quantities in an astrophysical context, we use the parameters derived from the X-ray observations of the Perseus Cluster as an example (Churazov et al. 2003). These values are also given in Table 1.

The system of dimensionless equations is integrated in time by using an upwind scheme (Li & Li 2003). Computations were performed on the parallel Linux clusters at Los Alamos National Laboratory.

2.2. *Initial and Boundary Conditions*

One key difference between this paper and Paper I is that we now introduce a nonuniform background medium. An isothermal model (King 1962) has been adopted to model a gravitationally stratified ambient medium. This is applicable, for example, to modeling the magnetic towers from AGNs in galaxy clusters.

The initial distributions of the background density ρ and gas pressure p are assumed to be

$$\rho = p = \left[1 + \left(\frac{R}{R_c}\right)^2\right]^{-\kappa}, \tag{5}$$

where $R = (x^2 + y^2 + z^2)^{1/2}$ is the spherical radius and R_c the cluster core radius. (In the following discussion, both "transverse" and "radial" have the same meaning, referring to the cylindrical radial direction.) The parameter κ controls the gradient of the ambient medium. Furthermore, we assume that the ambient gas is initially in hydrostatic equilibrium under a fixed (in time and space) yet distributed gravitational field $-\nabla\psi(R)$ (such as that generated by a dark matter potential). From the initial equilibrium, we get

$$-\nabla\psi = \frac{\nabla p|_{t=0}}{\rho|_{t=0}} = -\frac{2\kappa R}{R_c^2}\left[1 + \left(\frac{R}{R_c^2}\right)^2\right]^{-1}. \tag{6}$$

In the present paper, we choose $R_c = 4.0$ and $\kappa = 1.0$. The initial sound speed in the system is constant, $C_s|_{t=0} = \gamma^{1/2} \approx 1.29$, throughout the computational domain. An important timescale is the sound crossing time $\tau(\equiv R/C_s) \approx 0.78$, normalized with $\tau_{s0}(\equiv R_0/C_{s0}) \approx 10.0$ Myr. Therefore, a unit timescale $t = 1$ corresponds to 12.8 Myr.

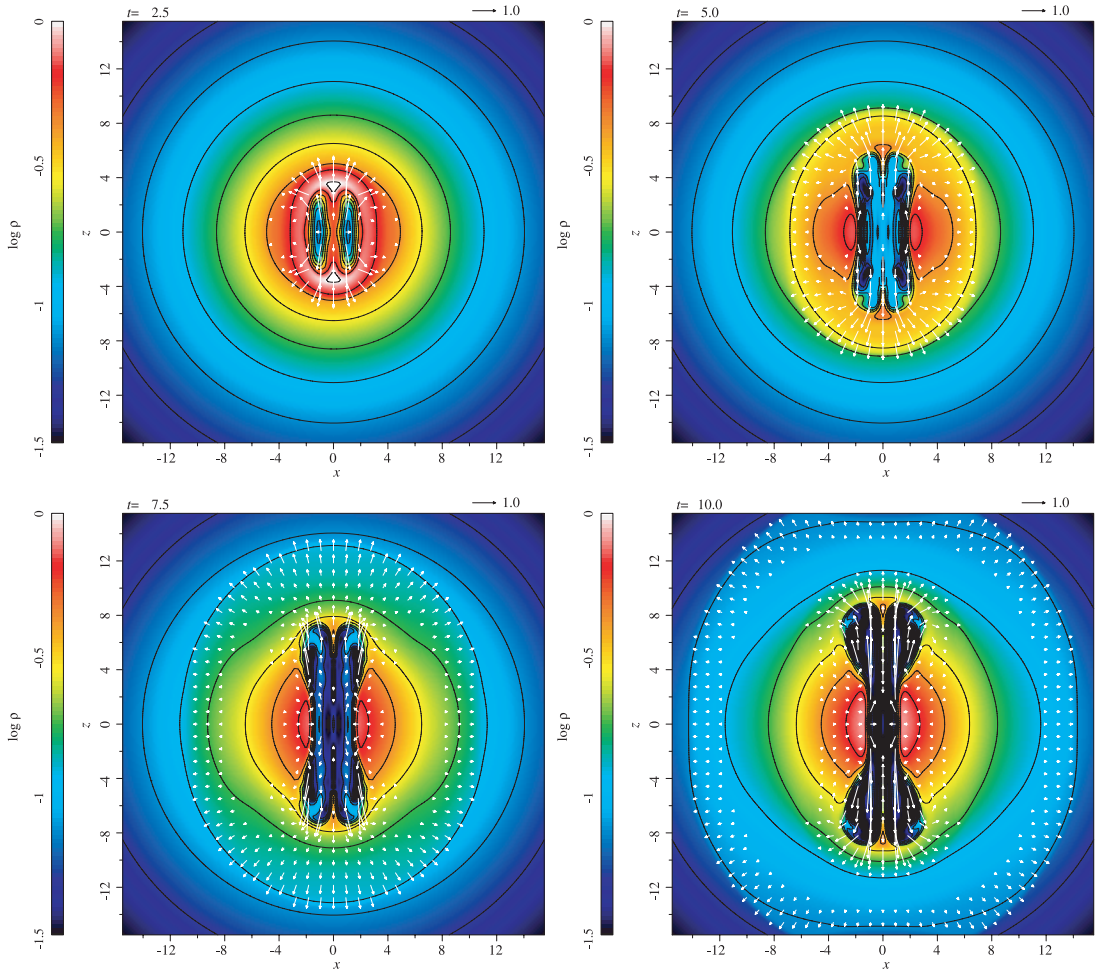


FIG. 1.—Density evolution caused by a magnetic tower jet propagating through a stratified background. The color scale and contours of the density distribution (in logarithmic scale) are shown along with the poloidal velocity field (*arrows*) in the *x*-*z* plane. Density cavities are formed due to the magnetic field expansion. Times are given at the upper left in each of the four panels. The length of the arrow at the upper right in each panel shows the unit velocity.

The total computational domain is taken to be $|x| \leq 16$, $|y| \leq 16$, and $|z| \leq 16$ corresponding to a $(160\ \mathrm{kpc})^3$ box in the actual length scales. The numbers of grid points in the simulations reported here are $N_x \times N_y \times N_z = 240 \times 240 \times 240$, where the grid points are assigned uniformly in the *x*-, *y*-, and *z*-directions. A cell Δx (=$\Delta y = \Delta z \sim 0.13$) corresponds to $\sim$0.67 kpc. We use the outflow boundary conditions at all outer boundaries. Note that for most of the simulation's duration, the waves and magnetic fields stay within the simulation box, and all magnetic fields are self-sustained by their internal currents.

2.3. *Injections of Magnetic Flux, Mass, and Energy*

The injections of magnetic flux, mass, and associated energies are the same as those described in Paper I. The ratio of the toroidal to poloidal fluxes of the injected fields is characterized by the parameter $\alpha = 15$, which corresponds to $\sim$6 times more toroidal flux than poloidal flux. The magnetic field injection rate is described by γ_b and is set to be 3. The mass is injected at a rate of $\gamma_\rho = 0.1$ over a central volume with a characteristic radius $r_\rho = 0.5$. Magnetic fields and mass are continuously injected for $t_{\mathrm{inj}} = 3.1$, after which the injection is turned off. These parameters correspond to a magnetic energy injection rate of $\sim 10^{43}$ ergs s^{-1}, a mass injection rate of $\sim 0.046\ M_\odot\ \mathrm{yr}^{-1}$, and an injection time of $\sim$40 Myr.

In summary, we have set up an initial stratified cluster medium that is in hydrostatic equilibrium. The magnetic flux and the mass are steadily injected in a central small volume with a radius of 1. Since these magnetic fields are not in a force-free equilibrium, they will evolve, forming a magnetic tower and interacting with the ambient medium.

3. RESULTS

In this section we examine the nonlinear evolution and the properties of magnetic tower jets in the gravitationally stratified atmosphere.

3.1. *Overview of Formation and Propagation of a Magnetic Tower Jet*

Before considering our numerical results in detail, it is instructive to give a brief overview of the time development of the magnetic tower jet system. We achieve this by presenting selected physical quantities using two-dimensional *x*-*z* slices at $y = 0$. The distributions of density at various times ($t = 2.5$, 5.0, 7.5, and 10.0) are shown in Figure 1. At the final stage ($t = 10.0$), we see the formation of a quasi-axisymmetric (around the jet axis) magnetic tower jet with low-density cavities (a factor of $\sim$30 smaller than the peak density). Inside these cavities, the Alfvén speed is large ($V_{\mathrm{A}} \gtrsim 5.0$), while plasma β is small ($\beta = 2p/B^2 \lesssim 0.1$).

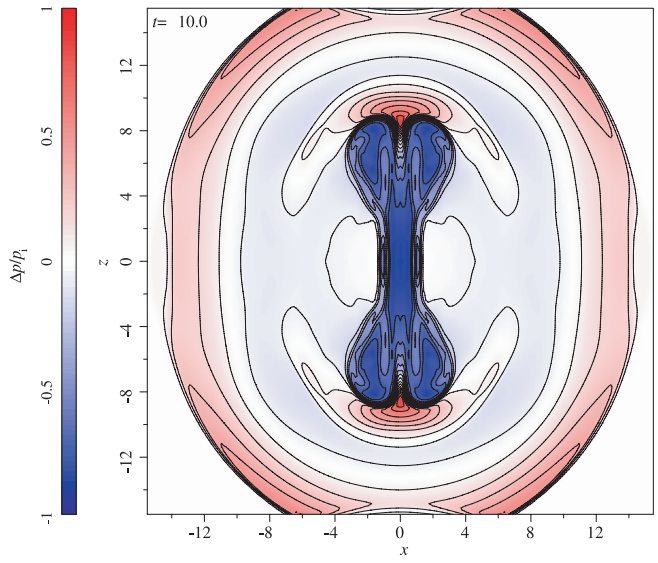


FIG. 2.—Change of the gas pressure $\Delta p/p_i$ ($\Delta p = p - p_i$; p_i represents $p|_{t=0}$) at $t = 10.0$ in the x-z plane.

However, the temperature $T(\propto C_s^2)$ becomes large ($T \gtrsim 2.5$, about twice the initial constant value); that is, the hotter gas is confined in the low-β magnetic tower. The jet possesses a slender hourglass-shaped structure with a radially confined "body" for $|z| \leq 3$, which is likely due to the background pressure profile having a core radius $R_c = 4$. As the magnetic tower moves into an increasingly lower pressure background, the expanded "lobes" are formed. A quasi-spherical hydrodynamic (HD) shock wave front moves ahead of the magnetic tower.

A snapshot of the gas pressure change ratio $\Delta p/p_i = p/p_i - 1$ (where p_i represents $p|_{t=0}$) at $t = 10.0$ is shown in Figure 2. Positive Δp can be seen both at the postshock region of the propagating HD shock wave and just ahead of the magnetic tower ($|z| \sim 8$–10). The distribution of $\Delta p/p_i$ forms a U-shaped bow shock–like structure around the head of the magnetic tower. This structure, however, does not appear until $t \sim 7.5$. This is apparently caused by the local compression between the head of the magnetic tower and the reverse MHD slow-mode wave (see discussions in § 3.2). The gas pressure inside the magnetic tower becomes small ($|\Delta p/p_i| \lesssim 0.5$) due to the magnetic flux expansion. Note that the light blue region between the HD shock and the magnetic tower shows a small pressure decrease ($\Delta p/p_i \approx -0.1$). In subsequent sections, we discuss the origin of this depression and what role it plays in the dynamics of magnetic tower jets.

The magnetic tower jet has a well-ordered helical magnetic configuration. The 3D view of the selected magnetic lines of force, as illustrated in Figure 3, indicates that a tightly wound central helix goes up along the central axis and a loosely wound helix comes back at the outer edge of the magnetic tower jet. The magnetic pitch $B_\phi/(B_r^2 + B_z^2)^{1/2}$ has a broad distribution with a maximum of $\sim$15. Figure 4 shows a snapshot of the axial current density J_z at $t = 10.0$. Clearly, the axial current flow displays a closed circulating current system in which it flows along the central axis (the "forward" current) and returns on the conical path that is on the outside (the "return" current). It is well known that an axial current-carrying cylindrical plasma column with a helical magnetic field is subject to current-driven instabilities, such as sausage ($m = 0$), kink ($m = 1$), and the other higher order m-modes (m is the azimuthal mode number). However, we do not

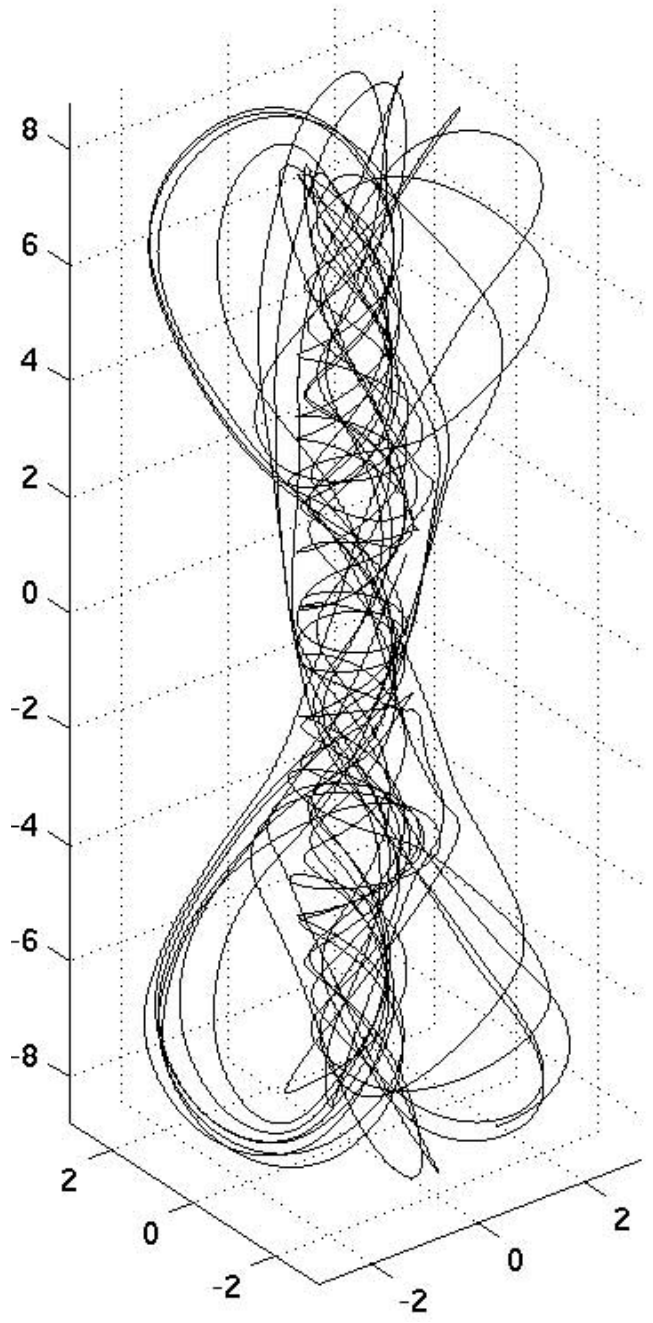


FIG. 3.—Three-dimensional configuration view of the selected magnetic lines at $t = 10.0$.

see any visible evolution of the nonaxisymmetric features in this magnetic tower jet.

From this overview, we see that the magnetic tower jet can propagate through the stratified background medium while keeping well-ordered structures throughout the time evolution. The magnetic fields push away the background gas, forming magnetically dominated, low-density cavities. This action also drives a HD shock wave that is ahead of and eventually separated from the magnetic structures. The magnetic tower has a slender body from the confinement of the background pressure and an expanded lobe when the fields expand into a background with decreasing pressure.

We now turn to the discussions on the detailed properties of the tower jet, including the HD shock wave and its impact in the

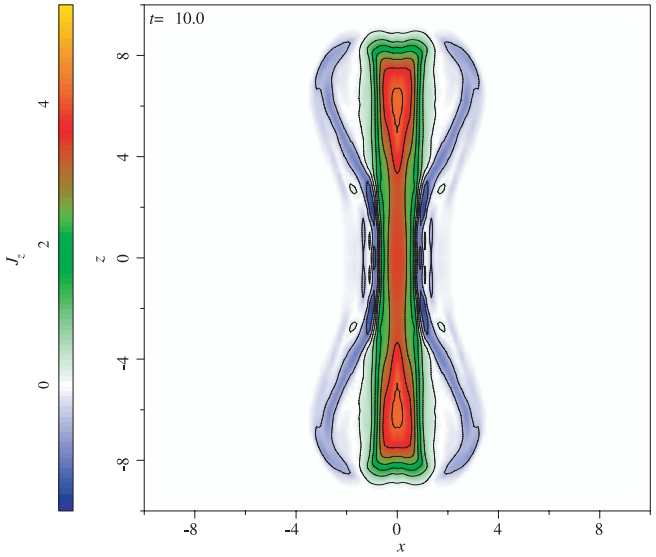


FIG. 4.—Distribution of the axial current density J_z at $t = 10.0$ in the x-z plane. It shows a closed circulating current system, in which the current flows along the central (z) column ($J_z > 0$) and returns along the conical shell on the outside ($J_z < 0$).

axial (z) and radial (x) directions in §§ 3.2 and 3.3. The radial force balance of the jet is examined in § 3.4.

3.2. *Structure of a Magnetic Tower Jet in the Axial (z) Direction*

Figure 5 displays several physical quantities along a line with $(x, y) = (1, 0)$ in the axial direction at $t = 0.75$. Several features can be identified. First, the HD shock wave front can be seen around $z \sim 13.5$ in the profiles of ρ (*top*), V_z, and C_s (*bottom*). The sound speed C_s is higher than the initial background value 1.29 in the postshock region due to shock heating and becomes smaller than 1.29 at $z \sim 10.7$ due to axial expansion; V_z shows similar behavior.

Second, a magnetic tower front ("tower front" in the following discussion) is located at $z \sim 8.0$, beyond which the magnetic field goes to zero, as seen in Figure 5 (*top*). This indicates that the gas within the magnetic tower jet is separated from the nonmagnetized ambient gas beyond the tower front. We refer to this front as a tangential discontinuity, since the magnetic fields are tangential to the front without the normal component. This is consistent with the fact that the radial and azimuthal field components (B_r and B_ϕ) are dominant near the tower front ($z \lesssim 8.0$) but the axial field component B_z becomes dominant only for $z < 6.0$. The density and pressure show smooth transition through this front, although the gradients of ρ and C_s are slightly changed there.

Third, there is another MHD wave front at $z \sim 7.0$ where B_r, C_s, and all the velocity components have their local maxima (ρ instead has its local minimum), as seen in both panels of Figure 5. To better understand the nature of this MHD wave front, we plot the axial profiles of the pressures and various forces along the line $(x, y) = (1, 0)$ at $t = 7.5$ in Figure 6. The total pressure $p_{\rm tot}$ consists of only the gas pressure p beyond the tower front ($z \gtrsim 8.0$) but is dominated by the magnetic pressure p_m behind the MHD wave front ($z \lesssim 7.0$), as seen in Figure 5 (*top*). A transition occurs around $7.0 \lesssim z \lesssim 8.0$, where an increase in p is accompanied by a decrease in p_m. We therefore identify this as a reverse slow-mode compressional MHD wave front. In magnetic towers, the transition region between gas and magnetic pressures can be identified as a reverse slow wave front in the context of MHD wave structures. It does not depend on the resolution and parameters. Thus, the reverse slow-mode wave (sometimes it can

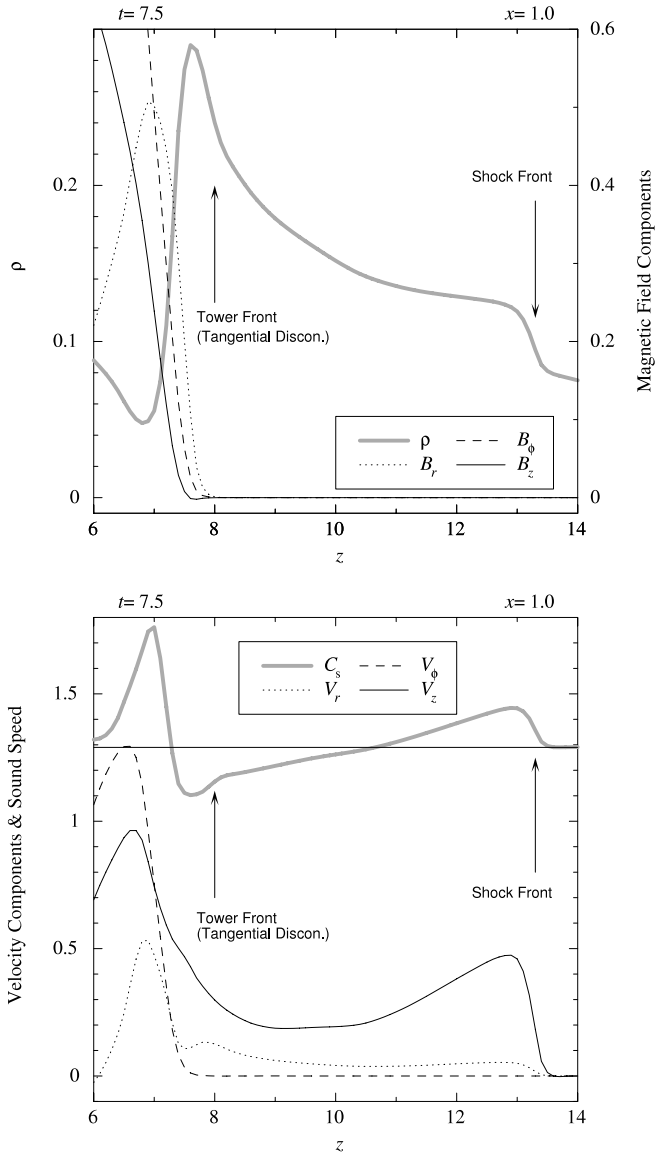


FIG. 5.—Axial profiles of physical quantities, parallel to the z-axis with $(x, y) = (1, 0)$ at $t = 7.5$. *Top:* Density ρ and magnetic field components (B_r, B_ϕ, B_z). *Bottom:* Sound speed C_s and velocity components (V_r, V_ϕ, V_z). The positions of the expanding hydrodynamic shock wave front and the magnetic tower front, which is identified as a tangential discontinuity, are shown in both panels. A horizontal solid line in the bottom panel denotes the initial sound speed (constant throughout the computational domain).

be steepen into a shock) will always be there. In addition, in Figure 7, we show several snapshots of V_z and p during $t = 7.5$–10.0 (along the same offset axial path as in Figs. 5 and 6). The axial flow is decelerated by the gravitational force in the postshock region beyond the tower front as seen in Figure 7 (*top*). On the other hand, the narrow region between the tower front and the reverse slow-mode wave front is accelerated by the magnetic pressure gradient (the "magnetic piston" effect). Note that the reverse slow-mode MHD compressional wave could eventually steepen into the reverse slow-mode MHD shock wave via this nonlinear evolution. Consequently, in the frame comoving with the reverse slow-mode shock, a strong compression occurs behind the shock wave front and causes a local heating, as seen in Figure 7 (*bottom*) and in Figure 2. This heating could have interesting implications for the enhancement of radiation from radio

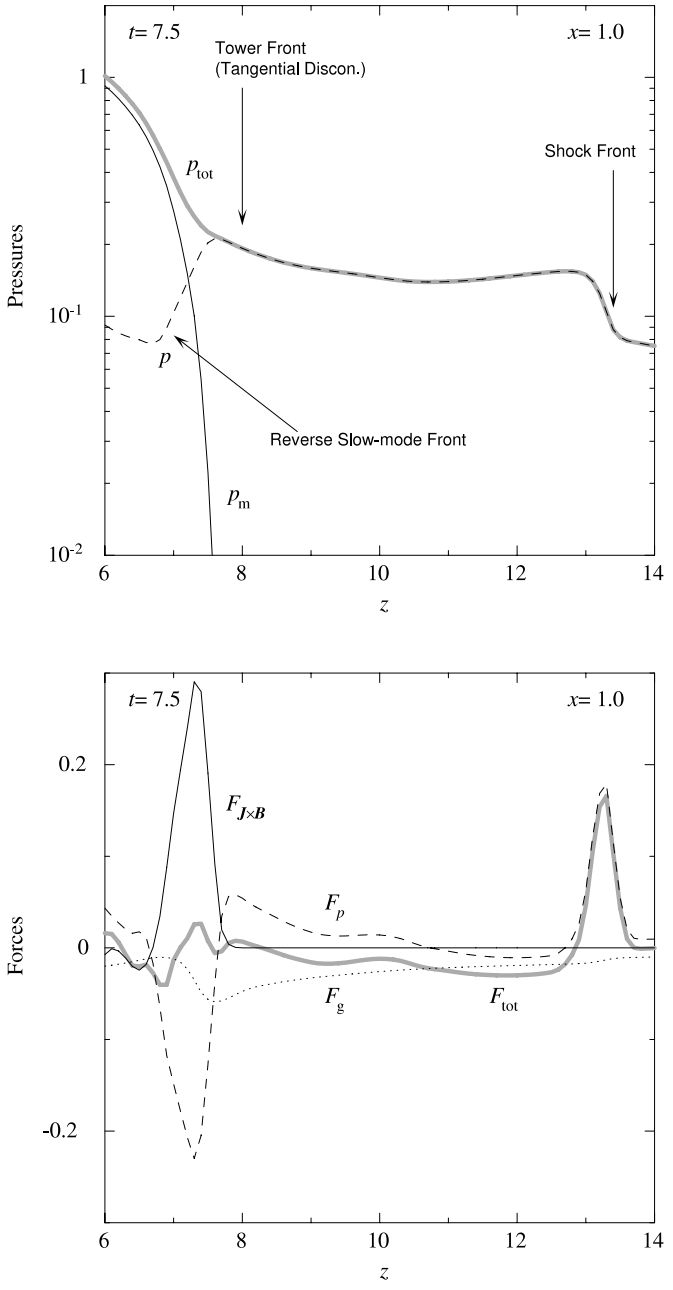


FIG. 6.—*Top:* Gas pressure p (*dashed line*), magnetic pressure p_m (*black thin solid line*), and total pressure $p_{\rm tot}$ ($=p+p_m$; *gray thick solid line*). *Bottom:* Forces in the axial (z) direction: Lorentz force $F_{\boldsymbol{J}\times\boldsymbol{B}}=-\partial/\partial z[(B_r^2+B_\phi^2)/2]$ (*black thin solid line*), gas pressure gradient force $F_p=-\partial p/\partial z$ (*dashed line*), gravitational force $F_g=-\rho(\partial\psi/\partial R)(|z|/R)$ (*dotted line*), and total force $F_{\rm tot}$ ($=F_{\boldsymbol{J}\times\boldsymbol{B}}+F_p+F_g$; *gray thick solid line*). The position of the reverse slow-mode MHD wave front is also shown in the top panel.

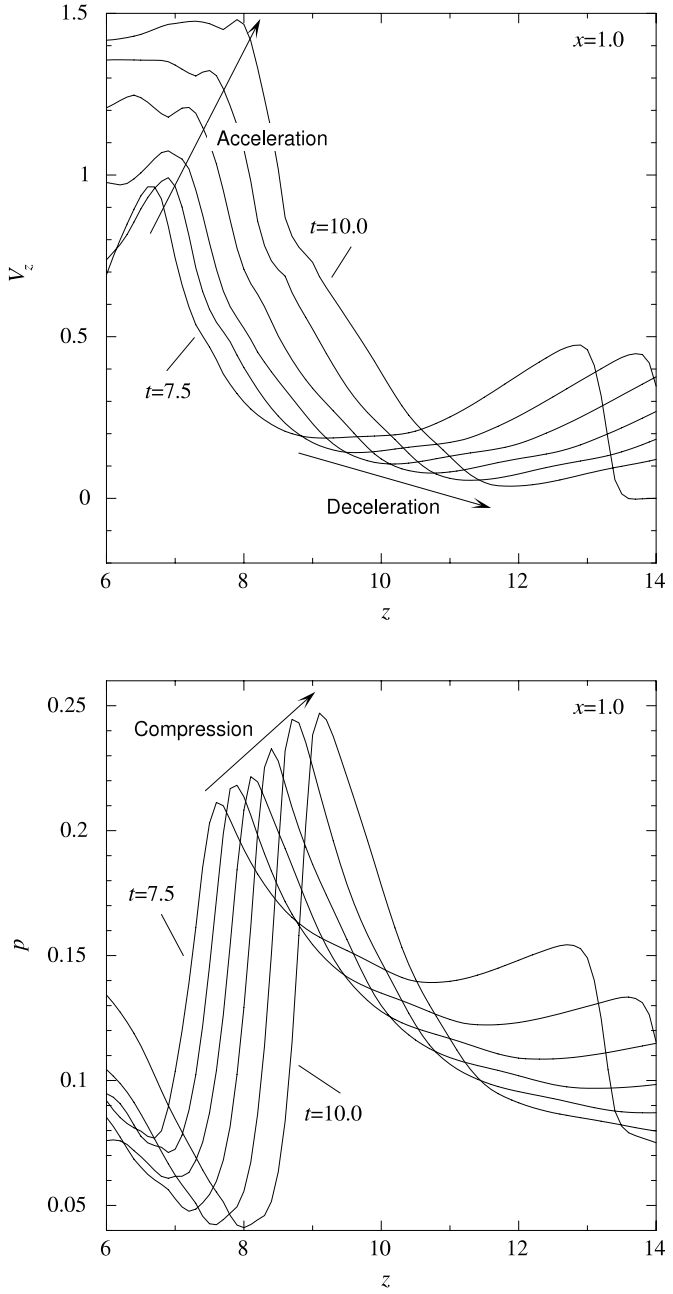


FIG. 7.—Same as Fig. 5, but with selected snapshots during $t=7.5$–10.0 (each time interval is equal to 0.5). *Top:* Axial velocity V_z. *Bottom:* Gas pressure p.

to X-rays at the terminal part of Fanaroff-Riley type II AGN jets, such as lobes and hot spots, which are generally interpreted as heating caused by the jet terminal shock wave (Blandford & Rees 1974; Scheuer 1974).

Fourth, the HD shock wave breaks the initial background hydrostatic equilibrium. The passage of the shock wave heats the gas and alters its pressure gradient. As shown in Figure 6 (*bottom*), the gas pressure gradient force F_p stays positive at the shock front (which pushes the shock forward), but the total (gravity plus pressure gradient) force $F_{\rm tot}$ becomes negative behind the shock, implying a deceleration of the gas in the axial direction in the postshock region. This is consistent with Figure 7.

3.3. *Deformation of the Jet Body in the Radial Direction*

We next examine the structure and dynamics of the magnetic tower jet along the radial direction in the equatorial plane with $(y,z)=(0,0)$. Figure 8 shows the radial profiles of physical quantities along the x-axis at $t=6.0$. The boundary of the magnetic tower jet ("tower edge" in the following discussion) is located at $x\sim3.0$ where $F_{\boldsymbol{J}\times\boldsymbol{B}}$ becomes zero. Two distinct peaks of C_s and V_x around $x\sim7.8$ and 9.5 are visible in Figure 8 (*top*). The first front ($x\sim9.5$) is the propagating HD shock wave front as we showed in the previous section. The second front ($x\sim7.8$) also indicates another expanding HD shock wave front generated by a bounce when the magnetic flux pinches in the radial direction caused by the "hoop stress." This secondary shock front appears only in the radial direction (see also Fig. 5). The sound speed C_s decreases gradually toward the jet axis in the postshock region of the

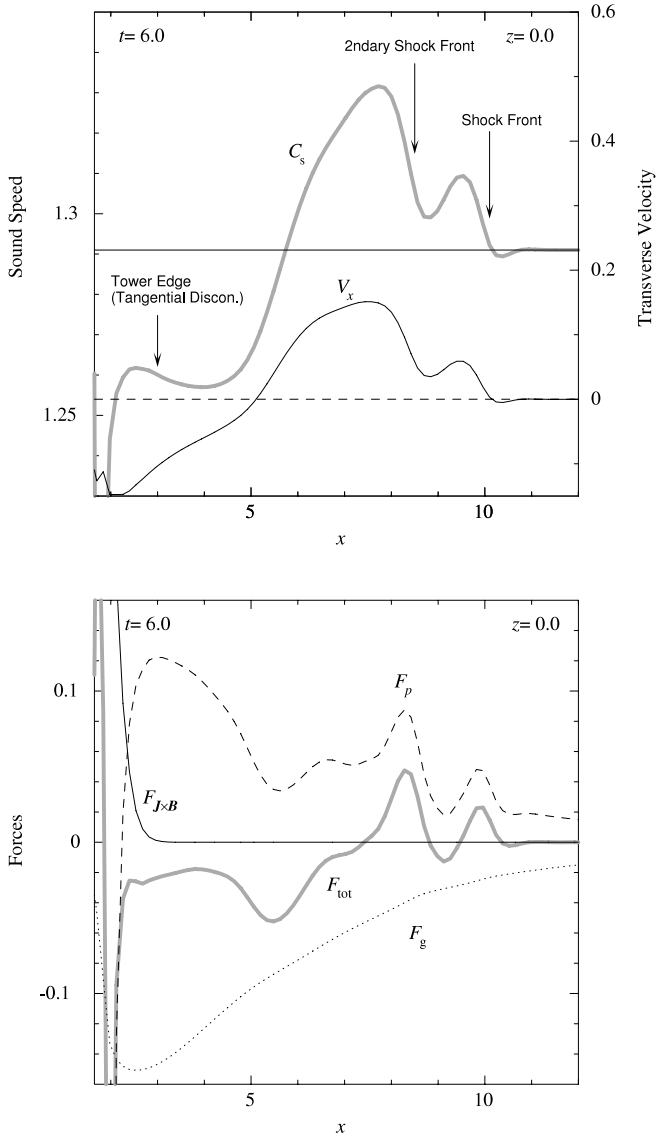


FIG. 8.—Radial profiles of physical quantities along the x-axis in the equatorial plane with $(y, z) = (0, 0)$ at $t = 6.0$. *Top:* Sound speed C_s (*gray thick solid line*) and radial velocity V_x (*black thin solid line*). *Bottom:* Forces in the radial (x) direction: Lorentz force $F_{\boldsymbol{J}\times\boldsymbol{B}} = -\partial/\partial r[(B_\phi^2 + B_z^2)/2] - B_\phi^2/r$ (*solid line*), gas pressure gradient force $F_p = -\partial p/\partial r$ (*dashed line*), gravitational force $F_g = -\rho(\partial\psi/\partial R)(|x|/R)$ (*dotted line*), and total force $F_{\rm tot}$ ($=F_{\boldsymbol{J}\times\boldsymbol{B}} + F_p + F_g$; *light gray thick solid line*). The positions of two expanding hydrodynamic shock wave fronts and the edge of the magnetic tower (tangential discontinuity) are shown in the top panel. A horizontal solid line in the top panel denotes the initial sound speed (constant throughout the computational domain), and a horizontal dashed line in the top panel represents level 0 for the transverse velocity.

secondary shock and becomes smaller than its initial value 1.29 at $x \sim 5.7$. We can confirm that these shock fronts are purely powered by the gas pressure gradients F_p, as seen in Figure 8 (*bottom*; twin peaks of F_p are shifted a bit behind that of C_s in the top panel).

The total force $F_{\rm tot}$ is negative in part of the region between the secondary HD shock front and the tower edge (Fig. 8, *bottom*), meaning that the gas is undergoing gravitational contraction. This is indicated by $V_x < 0$ in the top panel for $x < 5.1$. This behavior is similar to what we have discussed above; i.e., the HD shock waves break the background hydrostatic equilibrium, causing a global contraction. Note that this contraction is occurring along the whole jet body, e.g., for $|z| \lesssim 4.0$ when $t = 7.5$.

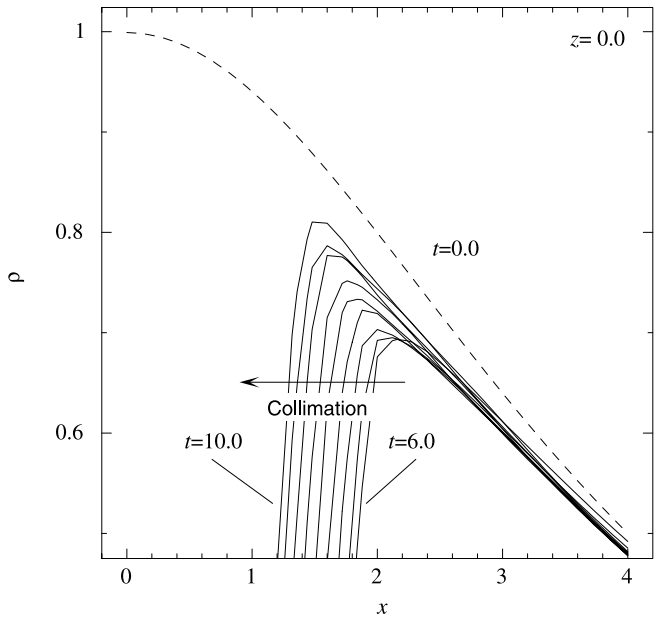


FIG. 9.—Radial profiles of density ρ in the equatorial plane with selected snapshots during $t = 6.0$–10.0 (each time interval is equal to 0.5). The initial profile ($t = 0.0$) is also shown (*dashed line*).

The bottom panel of Figure 8 also helps to address the question of which forces are confining the magnetic fields in the equatorial plane. Since the total magnetic field $F_{\boldsymbol{J}\times\boldsymbol{B}}$ stays positive, the inward hoop stress is not strong enough to confine the magnetic fields. Instead, at the tower edge, it is the background gravity that counters the combined effects of magnetic field pressure and a positive pressure gradient (pushing outward). A bit farther into the tower edge (at $x \sim 2.1$), however, the pressure force changes from outwardly directed to inwardly directed. Then both the pressure gradient and the gravitational forces act to counter the outward $\boldsymbol{J} \times \boldsymbol{B}$ force. This behavior, which is mostly caused by the magnetic tower expanding in a background gravitational field, is different from the usual MHD models for jets in which the inwardly directed hoop stress is balanced by the outwardly directed magnetic pressure gradient (Blandford & Payne 1982).

To investigate the radial evolution of the magnetic tower jet, we show the radial profile of density at the equatorial plane from $t = 6.0$ to 10.0 in Figure 9. The figure shows that the radius has an approximately constant contraction speed for $t = 6.5$–9.5. The timescale for contraction is $\tau_{\rm contr} \sim 6$, which is about 7.5 times longer than the local sound crossing time.

3.4. *Force Balance in the Radial Direction*

We now discuss the jet properties along the radial direction away from the equatorial plane. Figure 10 shows the radial profiles of physical quantities along the x-axis with $(y, z) = (0, 4)$ at $t = 7.5$. The tower edge is now located at $x \sim 3.0$. The plasma β in the core of the tower is $\beta \lesssim 0.1$. Figure 10 (*top*) shows that the central total pressure (which is dominated by the magnetic pressure) is much greater than the background "confining" pressure. This illustrates the original suggestion by Lynden-Bell (Lynden-Bell 1996, 2003) that the hoop stress of the toroidal field component B_ϕ can act as a pressure amplifier in the central region of the magnetic tower: the pinch effect amplifies p_m near the axis of the tower. At the tower edge, however, a finite (albeit small) gas pressure is required (see also Li et al. 2001).

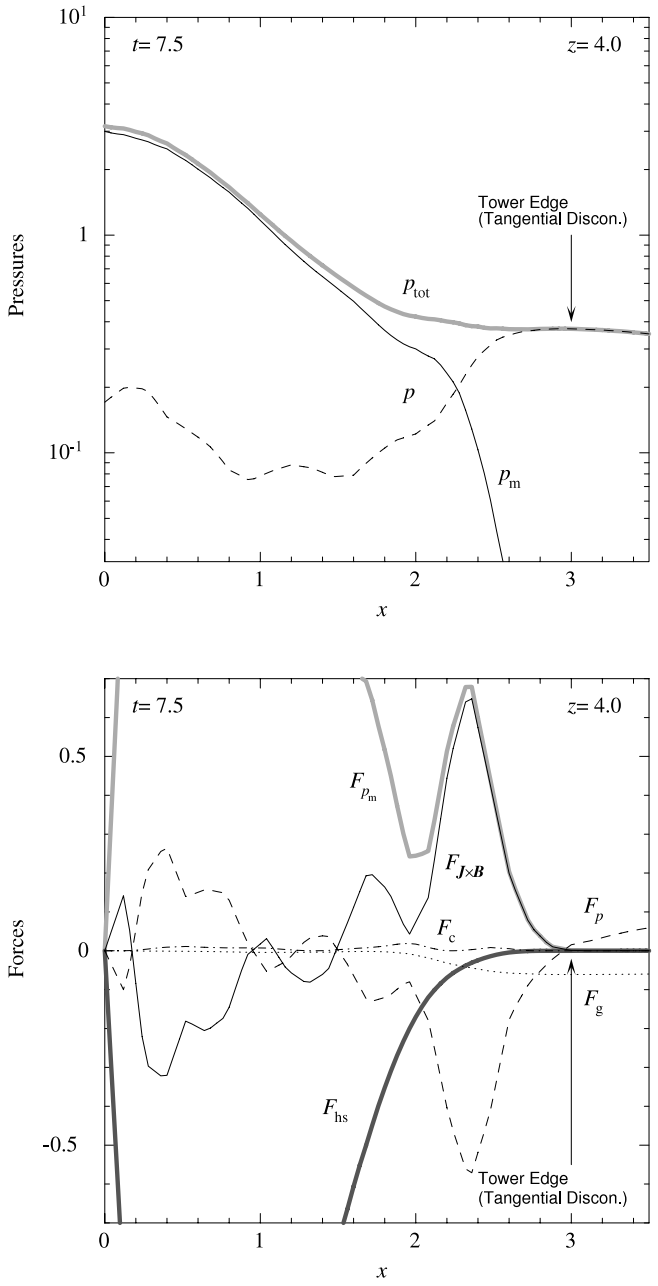


FIG. 10.—*Top:* Same as the top panel in Fig. 6, but showing the radial profiles of physical quantities along the x-axis with $(y,z) = (0,4)$ at $t = 7.5$. *Bottom:* Same as the bottom panel in Fig. 8, but with the centrifugal force $F_c = \rho V_\phi^2/r$ (*dash-dotted line*) and the Lorentz force $F_{\boldsymbol{J}\times\boldsymbol{B}}$, which can be separated into the magnetic pressure gradient force $-\partial/\partial r[(B_\phi^2 + B_z^2)/2]$ (*light gray thick solid line*) and the hoop stress (magnetic tension force) $-B_\phi^2/r$ (*dark gray thick solid line*). The position of the magnetic tower edge (tangential discontinuity) is shown in both panels.

The bottom panel of Figure 10 shows the detailed distributions of forces along the radial direction in the following regions.

Region $x \gtrsim 3.0$.—Beyond the tower edge, the gravitational force F_g is slightly stronger than the outwardly directed gas pressure gradient force F_p, indicating that this edge is subject to gravitational contraction, as discussed in § 3.3.

Region $2.0 \lesssim x \lesssim 3.0$.—Inside the tower edge, the Lorentz force $F_{\boldsymbol{J}\times\boldsymbol{B}}$ is dominated by the outwardly directed magnetic pressure gradient force F_{p_m} and is also larger than the inwardly directed F_p, indicating that the outer shell of the magnetic tower should be expanding at relatively higher z, in contrast to the equatorial region ($z = 0$), where the tower radius is contracting. The hoop stress $F_{\rm hp}$ plays a minor role in the force balance around this region. Note that the return current flows inside this region.

Region $x \lesssim 2.0$.—Inside the jet body, contributions from both F_{p_m} and $F_{\rm hp}$ become comparable and nearly cancel each other. The residual $F_{\boldsymbol{J}\times\boldsymbol{B}}$ is balanced by F_p everywhere in this region. The hoop stress $F_{\rm hp}$ becomes dominant in the Lorentz force at the core part. Note that the forward current flows within $x \lesssim 1.0$.

In addition, both F_g and the centrifugal force F_c play a minor role in terms of the force balance inside the magnetic tower jet. Thus, the interior of the magnetic tower is magnetically dominated but not exactly force-free; i.e., $-\nabla p + \boldsymbol{J}\times\boldsymbol{B} \simeq 0$. This small but finite pressure gradient force could potentially provide some stabilizing effects on the traditionally kink-unstable twisted magnetic configurations. The stability properties in magnetic tower jets will be examined in detail in a forthcoming paper.

4. DISCUSSIONS

On scales of approximately tens to hundreds of kiloparsecs, the background density and pressure profiles have a strong influence on the overall morphology of the magnetic tower jet. Most notably, the transverse size of the magnetic tower grows as the jet propagates into a decreasing pressure environment, showing a similar morphology with the jet/lobe configuration of radio galaxies.

The radial size of the lobe $r_{\rm lobe}$ can be estimated from the following consideration: Figure 11 shows the radial profiles of magnetic field components parallel to the x-axis with $z = 7.0$ at $t = 10.0$. Together with Figure 4, we see that both the poloidal field and especially the poloidal current I_z remain well collimated around the central axis even at a late stage of the evolution. This implies that the toroidal magnetic fields in the lobe region are distributed roughly as $B_\phi \sim I_z/r$. This is consistent with the results shown in Figure 11, where rB_ϕ have a plateau from $x \approx 1$ to ≈ 2.5. As indicated in Figure 10, we see that the magnetic pressure

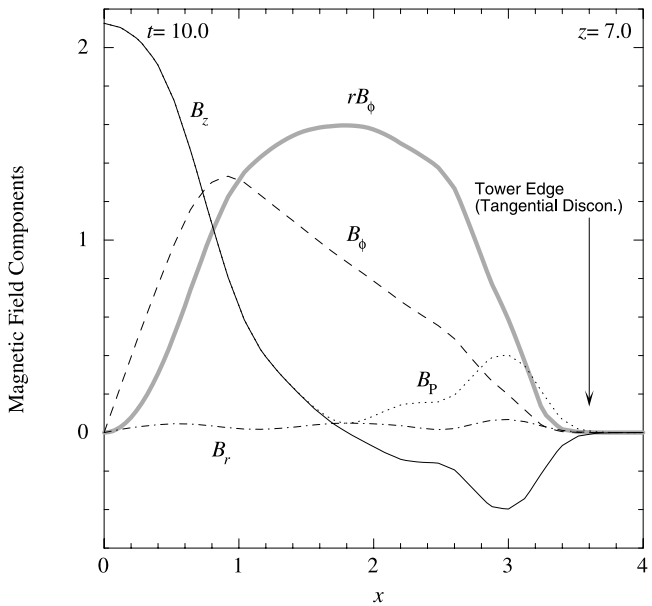


FIG. 11.—Radial profiles of the magnetic field components (B_r, B_ϕ, B_z), the poloidal magnetic field $B_p = (B_r^2 + B_z^2)^{1/2}$, and the quantity rB_ϕ along the x-axis with $(y,z) = (0,7)$ at $t = 10.0$. The position of the magnetic tower edge (tangential discontinuity) is shown.

and the background pressure try to balance each other at the tower edge. Thus, we expect that

$$\frac{B_P^2 + B_\phi^2}{8\pi} \sim p_e, \tag{7}$$

where p_e is the external gas pressure at the tower edge. When the lobe experiences sufficient expansion, we expect the poloidal field strength to drop much faster than $1/r_{\rm lobe}$. So we have

$$\frac{B_\phi^2}{8\pi} \sim \frac{(I_z/r_{\rm lobe})^2}{8\pi} \sim p_e, \tag{8}$$

which gives

$$r_{\rm lobe} \sim I_z p_e^{-1/2}. \tag{9}$$

This is generally consistent with our numerical result shown in Figure 1, although it is difficult to make a firm quantitative determination, since the lobes have not expanded sufficiently.

To make direct comparison between our simulations and observations, further analysis is clearly needed. Note that for the magnetic tower model, the Alfvén surface is located at the outer edge of the magnetic tower and flow within the magnetic tower is always sub-Alfvénic. This is quite different from the hydromagnetic models in which the MHD flow is accelerated and has passed through several critical velocity surfaces, including the Alfvén surface.

5. CONCLUSION

By performing 3D MHD simulations we have investigated in detail the nonlinear dynamics of magnetic tower jets, which propagate through the stably stratified background that is initially in hydrostatic equilibrium. Our simulations, based on the approach developed in Li et al. (2006), confirm a number of the global characteristics developed in Lynden-Bell (1996, 2003) and Li et al. (2001). The results presented here give additional details for a dynamically evolving jet in a stratified background. The magnetic tower is made of helical magnetic fields, with poloidal flux and poloidal current concentrated around the central axis. The "returning" portion of the poloidal flux and current is distributed on the outer shell of the magnetic tower. Together they form a self-contained system with magnetic fields and associated currents, being confined by the ambient pressure and gravity. The overall morphology exhibits a confined magnetic jet "body" with an expanded "lobe." The confinement of the body comes jointly from the external pressure and the gravity. The formation of the lobe is due to the expansion of magnetic fields in a decreasing background pressure.

A hydrodynamic shock wave initiated by the injection of magnetic fluxes propagates ahead of the magnetic tower and can break the hydrostatic equilibrium of the ambient medium, causing a global gravitational contraction. As a result, a strong compression occurs in the axial direction between the magnetic tower front and the reverse slow-mode MHD shock wave front that follows. Furthermore, the magnetic tower jets are deformed radially into a slender body due to the inward-directed flow of the ambient (nonmagnetized) gas.

The lobe is magnetically dominated and likely filled with the toroidal magnetic fields generated by the central poloidal current. At the edge of the magnetic tower jet, the outward-directed magnetic pressure gradient force is balanced by the inward-directed gas pressure gradient force, so the radial width of the magnetic tower can be determined jointly by the magnitude of the poloidal current and the magnitude of the external gas pressure. The highly wound helical magnetic field in the magnetic tower never precisely reaches the force-free equilibrium but obtains radial force balance, including with the gas pressure gradient inside the magnetic tower. The stability of the magnetic tower jets will be considered in our forthcoming papers.

Useful discussions with John Finn, Stirling Colgate, and Ken Fowler are gratefully acknowledged. This work was carried out under the auspices of the National Nuclear Security Administration of the US Department of Energy at Los Alamos National Laboratory (LANL) under contract DE-AC52-06NA25396. It was supported by the Laboratory Directed Research and Development Program at LANL and by the Institute of Geophysics and Planetary Physics (IGPP) at LANL.

REFERENCES

Blandford, R. D. 1976, MNRAS, 176, 465
Blandford, R. D., & Payne, D. G. 1982, MNRAS, 199, 883
Blandford, R. D., & Rees, M. J. 1974, MNRAS, 169, 395
Blandford, R. D., & Znajek, R. L. 1977, MNRAS, 179, 433
Churazov, E., Forman, W., Jones, C., & Böhringer, H. 2003, ApJ, 590, 225
Ferrari, A. 1998, ARA&A, 36, 539
Hsu, S. C., & Bellan, P. M. 2002, MNRAS, 334, 257
Kato, Y., Hayashi, M. R., & Matsumoto, R. 2004, ApJ, 600, 338
Kato, Y., Mineshige, S., & Shibata, K. 2004, ApJ, 605, 307
King, I. 1962, AJ, 67, 471
Kudoh, T., Matsumoto, R., & Shibata, K. 2002, PASJ, 54, 267
Lebedev, S. V., et al. 2005, MNRAS, 361, 97
Li, H., Lapenta, G., Finn, J. M., Li, S., & Colgate, S. A. 2006, ApJ, 643, 92 (Paper I)
Li, H., Lovelace, R. V. E., Finn, J. M., & Colgate, S. A. 2001, ApJ, 561, 915
Li, S., & Li, H. 2003, Technical Report LA-UR-03-8935 (Los Alamos: Los Alamos National Laboratory)
Lovelace, R. V. E. 1976, Nature, 262, 649
Lovelace, R. V. E., Li, H., Koldoba, A. V., Ustyugova, G. V., & Romanova, M. M. 2002, ApJ, 572, 445
Lovelace, R. V. E., & Romanova, M. M. 2003, ApJ, 596, L159
Lynden-Bell, D. 1996, MNRAS, 279, 389
———. 2003, MNRAS, 341, 1360
———. 2006, MNRAS, 369, 1167
Lynden-Bell, D., & Boily, C. 1994, MNRAS, 267, 146
Meier, D. L., Koide, S., & Uchida, Y. 2001, Science, 291, 84
Romanova, M. M., Ustyugova, G. V., Koldoba, A. V., Chechetkin, V. M., & Lovelace, R. V. E. 1998, ApJ, 500, 703
Scheuer, P. A. G. 1974, MNRAS, 166, 513
Turner, N. J., Bodenheimer, P., & Różyczka, M. 1999, ApJ, 524, 129
Uchida, Y., & Shibata, K. 1985, PASJ, 37, 515
Ustyugova, G. V., Lovelace, R. V. E., Romanova, M. M., Li, H., & Colgate, S. A. 2000, ApJ, 541, L21
Uzdensky, D. A., & MacFadyen, A. I. 2006, ApJ, 647, 1192